Comprehensive Vibration Analysis and Modeling for ZY-3 Satellite's Lifecycle

Fan Mo[a,b], Junfeng Xie[a,*], Shuyi Wang[c], Liping Zhao[a], Xiang Li[a,d], Haoran Xia[a], Yongjie Shang[e]

[a] Land Satellite Remote Sensing Application Center, Ministry of Natural Resources, No.1 Baishengcun, Zizhuyuan, Haidian District, Beijing, 100048, China
[b] School of Earth Sciences and Engineering, Hohai University, No.8 Focheng West Road, Jiangning District, Nanjing, 211100, China
[c] Beijing Institute of Control Engineering, Space City, Dengzhuang North Road, Haidian District, Beijing, 100094, China
[d] Wuhan University, 16 Luojiashan Road, Wuchang District, Wuhan, 430072, China
[e] The First Geodetic Survey Team, Ministry of Natural Resources, 38 Dameng East Road, Beilin District, Xi 'an, 710054, China
* Corresponding author. E-mail addresses: mof@lasac.cn (F. Mo), xiejf@lasac.cn (J. Xie).

Keywords: ZY-3 lifecycle; Vibration detection; Frequency; Amplitude; Modeling

Abstract

A stable platform environment is essential for achieving high-quality imaging and accurate attitude measurement of the ZY-3's stereo camera. It serves as the fundamental guarantee for the satellite's high geometric precision. Throughout its orbital operation, the platform encounters periodic vibrational occurrences resulting from internal load mechanics and significant external environmental variations, thereby impeding the high-fidelity collection of information by the satellite payload. The detection and modeling of vibrations are crucial tasks for the satellite ground system, as they provide reliable parameter inputs for optimizing attitude accuracy and image quality. This paper presents a method for developing a comprehensive frequency variation vibrational model of the ZY-3 satellite platform throughout its lifecycle, utilizing the inertial gyroscopes (gyros) data of the ZY-3 satellite. The instrument has identified vibrations at three specific frequencies: 0.21 Hz, 0.56 Hz, and 1.12 Hz, each with amplitudes of 0.07″, 0.04″, and 0.04″, respectively. Additionally, it has detected two fluctuating frequencies around 0.3 Hz and 0.6Hz. The period of frequency variation is approximately one year, with vibration ranges of (0.267, 0.299) and (0.603, 0.695). Following a malfunction of the solar panels on the satellite, there has been a shift in the vibration range. Moreover, as the satellite's on-orbit duration increases, this range is also undergoing gradual changes.

1. Introduction

Satellite platform vibration is characterized by the instability in attitude and periodic minor vibrations that manifest during the orbital operation of the satellite. The phenomenon emerges as a result of a confluence of diverse internal and external factors, including the satellite's structure, control systems, and gravitational perturbations(Tong et al., 2014 , Kirk et al., 2008 , Teshima and Iwasaki, 2007 , Tong et al., 2015a). The vibrations experienced by satellite platforms exhibit specific characteristics: they are characterized by low energy levels that do not cause structural damage to the satellite; higher resolution cameras are more susceptible to jitter; these vibrations have small amplitudes and a wide frequency band, posing challenges for accurate measurement (Toyoshima et al., 2010). Despite the relatively small magnitude of the vibration, it has a continuous impact on the satellite's geographic positioning and orientation(Pan et al., 2017 , Wang et al., 2017). Platform vibrations result in subtle fluctuations in the satellite's orientation at various times, which are evident in the satellite imagery. These fluctuations can lead to challenges such as inconsistent image stitching, imprecise geometric alignment, and reduced image quality (Chen et al., 2017 , Mattson et al., 2011). Consequently, these issues can impact the usability of image data in disciplines such as geographic information systems, cartography, environmental monitoring, and analysis of natural disasters(Ayoub et al., 2008). Therefore, the detection and modeling of satellite vibrations are of critical importance.

The ZY-3 satellite represents China's inaugural civilian high-resolution stereo mapping satellite, which combines mapping and resource survey capabilities (Cao et al., 2012). Launched on January 9, 2012, the satellite is equipped with three panchromatic three-line array stereo mapping cameras (fore, nadir, and aft) designed to precisely capture three-dimensional terrestrial coordinates of the images (Gao et al., 2016). This capability enables the production of 1:50,000 mapping products and facilitates the mapping and updating of large-scale topographic maps (Wang et al., 2016). The ZY-3 satellite is outfitted with three star-sensors and four sets of gyroscopes (gyros), creating a high-precision ground-based satellite attitude determination system. The satellite platform utilizes a combination of star sensors and gyros to accurately determine its attitude, with a sampling frequency of 4 Hz(Tong et al., 2015b , Tang et al., 2013). The ZY-3 satellite application system integrates platform vibration into the data processing to guarantee the quality of satellite mapping products through two technical levels: image quality enhancement and satellite attitude optimization. The ZY-3 satellite was originally intended to operate for 4 years. However, as of January 9, 2021, it has been in orbit for 9 years, exceeding its expected lifespan by 5 years. During this extended period, its mapping capability has significantly deteriorated, indicating that it has essentially reached the end of its service life.

Significant progress has been made by domestic scholars in the field of vibration detection for the ZY-3 satellite platform. Both Tongji University and Wuhan University have employed the imaging parallax of the ZY-3's multispectral images to carry out vibration detection experiments on the satellite platform. Research findings suggest the presence of a vibrational phenomenon at approximately 0.6Hz in the ZY-3 platform, with the amplitude of vibration being greater in the radial direction than in the along-track direction (Zhu et al., 2015). Tong introduced a method for detecting satellite vibrations using data processing from multiple sensors. The study revealed that the ZY-3 satellite's vibration frequency consistently hovers around 0.6-0.7 Hz (Tong et al., 2017). Furthermore, Tong estimated the vibration data of the ZY-3 satellite through phase correlation analysis (Tong et al., 2018). Zhang et al. employed virtual control points to compute the image residuals by comparing back-projected image points with virtual image points (Zhang et al., 2018). This approach facilitated the assessment of variations in satellite attitude, leading to the confirmation of 0.65 Hz attitude vibrations in the ZY-3 satellite. Liu introduced a method for detecting attitude vibration using images and dense ground control (Liu et al., 2016), (Ye et al., 2020). The effectiveness of

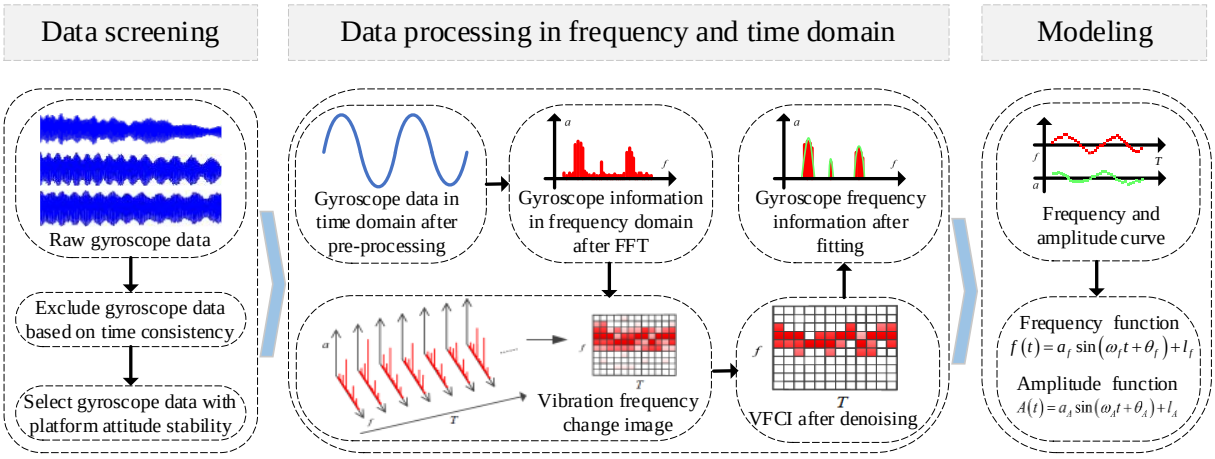

Figure1. Workflow for vibration modeling of the ZY-3 satellite platform.

this method was validated through case studies on the ZY-3 satellite, revealing a nearly constant vibration frequency of approximately 0.65 Hz. Upon synthesizing the findings of scholarly research, it has been established that the ZY-3 satellite platform exhibits a vibrational frequency of approximately 0.65 Hz, and this frequency has been observed to be variable. However, there is a dearth of technical research on the extent of variation in the vibration frequency of the ZY-3 satellite.

This paper presents a method for detecting and modeling vibration frequency changes in the ZY-3 satellite platform. The method utilizes the original gyro data collected throughout the entire lifecycle of the ZY-3 satellite. This study examines the patterns of variation in satellite platform vibration by analyzing long time series and a large amount of satellite gyro data. It develops a frequency-changing vibration model for the platform. This approach has successfully detected and modeled platform vibration across the entire lifecycle of the ZY-3 satellite.

2. Methodology

The ZY-3 satellite is outfitted with a high-precision attitude measurement system, which includes high-precision star sensors and three-floated gyros. The on-board gyros autonomously record changes in attitude during attitude maneuvers. The gyro data from the entire cycle of the ZY-3 satellite platform is utilized to enhance the precision and comprehensiveness of vibration information detection, as well as to develop a model for frequency variation. The workflow, depicted in Figure.1, comprises three stages that encompass the complete process of acquiring satellite platform vibration data and developing a model.

During the initial stage, gyro data that exhibits stability and is appropriate for modeling is chosen based on its time consistency and platform stability. In the second stage, the data selected undergo preprocessing using polynomials to reduce the influence of linear variations. Meanwhile, the results of fast Fourier transform (FFT) are used to divide frequency components in order to obtain vibration frequency changing image (VFCI). Gaussian low-pass filtering (GLPF) is employed to remove spurious noise in VFCI image and enhance the visibility of the multiple two-dimensional curves in VFCI. Subsequently, multi-segment parabolic fitting is employed to analyze the vibration amplitudes, with the aim of retaining the amplitudes within the parabolic curves and eliminating the outer sections for additional noise reduction. Subsequently, all time series fittings and frequencies are organized in a sequential manner to derive the frequency change curve. Similarly, the amplitude change curve can be obtained in a similar fashion. During the third stage, trigonometric functions are employed to model the frequency and amplitude change curves, thereby deriving the parameters for the vibration frequency and amplitude changes of the satellite platform. Ultimately, a comprehensive vibration model for the ZY-3 satellite platform is developed throughout its lifecycle.

2.1 Data screening

A gyro, also known as an angular velocity sensor, functions primarily based on the principle of conservation of angular momentum. This principle asserts that the angular momentum of an object remains constant when it rotates around an axis. This principle is employed for the determination of the rotational speed of an object (Xiong et al., 2011 , Yuan et al., 2012).

The gyro ascertains the orientation of the object by gauging the rotational angular velocity around its axis. The gyro measures the rotational speed of the object when it rotates. By integrating the rotational speed, the rotational angle, and consequently the object's attitude can be ascertained.

Gyro observation model can be expressed as follows:

$$\left.\begin{aligned}\omega_{gx} &= \omega_x + b_x + d_x + w_x \\ \omega_{gy} &= \omega_y + b_y + d_y + w_y \\ \omega_{gz} &= \omega_z + b_z + d_y + w_z\end{aligned}\right\} \quad (1)$$

where x, y, z are the gyro observation coordinate system; $\omega_{gi}(i = x, y, z)$ is the measured value of the gyro; $\omega_i(i = x, y, z)$ is the theoretical value of the gyro, $b_i(i = x, y, z)$ is the constant drift; $d_i(i = x, y, z)$ is the correlated drift; and $w_i(i = x, y, z)$ is the measurement random noise.

Original gyro data ω_{gi} is stored in the form of a time series.

Ideally, the distribution of gyro data over time is expected to be uniform. However, the gyro data may display anomalies or experience data loss as a result of noise, variations in environmental conditions, interference from motion, and transmission errors, all of which can subsequently compromise the dependability of vibration analysis on satellite platforms (Guo et al., 2017 , Mo et al., 2020). This study presents a detection and screening method for raw gyro data, focusing on time consistency. The gyros installed on the satellite integrate at a consistent sampling interval to acquire three-axis angular velocity data of the satellite at a fixed frequency. Consequently, the time interval between successive data points is consistently uniform. The occurrence of data loss

disrupts this consistency. The deletion or correction of these data points is necessary to complete the process of data detection and screening.

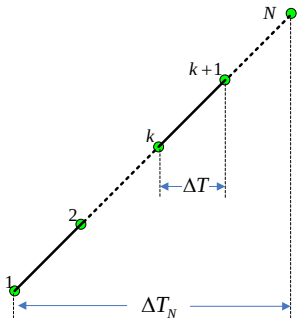

Figure.2 Temporal cohesion of satellite gyro data.

In Figure.2, the interval between adjacent data acquisition times is ΔT with N sets of data. The total acquisition time ΔT_N equals the number of data points N multiplied by ΔT. As indicated in Equation (1), temporal continuity of the data is contingent upon the simultaneous satisfaction of Equation (2) by all data points.

$$\begin{cases} T_{k+1} - T_k = \Delta T \\ T_N - T_1 = \Delta T_N \end{cases} \tag{2}$$

Under stable conditions, the gyro records the vibration status of the satellite platform, providing accurate information on factors such as the platform's vibration frequency. However, abnormal vibrations of the satellite platform may occur due to a variety of factors, including unconventional external forces and control torque affecting gyro operation. The gyro captures data that includes non-traditional frequency information, potentially impacting the ultimate outcomes of the experiment. In order to guarantee the precision of the experiment, the planned stability of the satellite platform is regarded as a crucial limitation. When the gyro measures changes in angle, it is essential for the data to satisfy the criteria for angle change stability in order to minimize input errors, and to guarantee the precision of the experiment and the credibility of the modeling.

$$S = \sqrt{\sum_{i=1}^{N}(g_i - g_{ave})^2} \tag{3}$$

where s is the platform stability calculated from gyro data; $i = 1, 2, 3, \cdots, N$ is the sequence number of the gyro data; N is the total number of gyro data points; g_i is the gyro data value; and g_{ave} is the mean value of the gyro data.

In Equation (3), if the stability of a given set of gyro data significantly exceeds the designated platform stability value (typically by a factor of 10), the data is deemed unusable and should be removed.

2.2 Data processing in frequency and time domain

2.2.1 Gyro Information in Frequency Domain after FFT: Gyros are commonly subject to system drift, charac terized by a linear or non-linear alteration in the gyro o utput that is independent of external stimuli or physical quantities. To address this issue, polynomial fitting of g yro data is employed to eliminate system drift from the raw data, resulting in more precise angular velocity mea surements. A general polynomial is represented as shown in Equation (4).

$$f(x) = a_0 + a_1 x + \cdots + a_n x^n \tag{4}$$

where $f(x)$ is the fitting result; $a_0 \sim a_n$ is the fitting coefficient; and n is the order of fitting.

In cases where the precision requirements for attitude determination on satellites are not stringent, this approach is frequently employed to better fit and smooth satellite attitude, thereby reducing noise and jitter in the data. This results in acquired attitude data that is more readily analyzable and visualizable.

Fourier transform, also referred to as Fourier analysis, serves as a mathematical instrument for signal analysis, facilitating the linkage between the time domain and the frequency domain (Ye et al., 2019 , Chen et al., 2001 , Sun et al., 2015). This connection allows for enhanced examination of the frequency and periodic attributes of intricate signals. The mathematical equation is represented by Equation (5).

$$F(u) = \int_{-\infty}^{\infty} f(t) e^{-j2\pi ut} dt \tag{5}$$

where $F(u)$ is the frequency domain value; $f(t)$ is the time domain value; t is the time; u is the frequency; and j is the imaginary part of a complex number.

By utilizing general polynomials and FFT, it is possible to convert gyro data from the time domain to the frequency domain, enabling analysis and extraction of information regarding the satellite platform's frequency, amplitude, and phase.

2.2.2 Vibration frequency change image: The frequency and amplitude spectra of a single track of gyro data are acquired following FFT analysis. The spectra encompass information regarding both frequency and amplitude. The gyros are activated solely during camera scanning, resulting in frequency spectra that only capture frequency information at approximately 10-minute intervals. The short-term analysis fails to adequately demonstrate fluctuations in vibration. To identify and analyze long-term changes in vibration frequency, this study develops VFCI using a series of gyro frequency spectra.

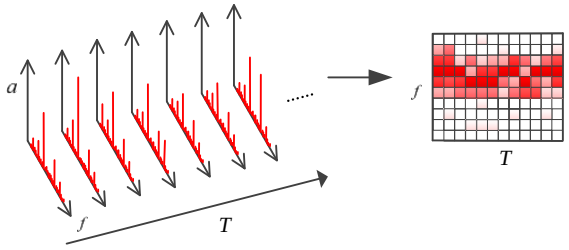

Figure.3 Representation of frequency variations in satellite vibration data.

The schematic diagram of VFCI is depicted in Figure.6. The diagram on the left depicts a collection of two-dimensional frequency spectra. The horizontal axis in this context denotes frequency, while the vertical axis signifies amplitude. The illustration on the right depicts VFCI, where time is represented on the horizontal axis, frequency on the vertical axis, and different colors indicate amplitude intensity.

In VFCI illustration, the detection result of one gyro's data, represented by the frequency spectrum in the left portion of Figure.6, is arranged as a column in the right grid. The gray intensity value of VFCI corresponds to the vertical axis variable in the two-dimensional frequency spectra, thereby indicating vibration amplitude. VFCI provides a means to obtain the frequency changes of various vibrations in the satellite platform.

2.2.3 VFCI denoising: VFCI displays the satellite platform's long-term vibration frequency, with the gray pixels indicating the amplitude of vibration. Due to the variable nature of vibration amplitude, which can be influenced by various factors, noise is present in VFCI. The presence of this noise could potentially impact the modeling of the frequency change curve. In order to mitigate this influence, the utilization of image processing technology is essential for enhancing VFCI before modeling.

VFCI is an image comprised of two-dimensional frequency spectra. The two-dimensional frequency spectra represent the frequency information of the raw gyro data. The gyro data in space are subject to influence from various factors. Furthermore, the primary frequencies of vibration in satellite platforms consist of several constant values. Consequently, the two-dimensional frequency spectra encompass low-frequency vibration data alongside high-frequency noise. In order to reduce the high-frequency noise, a GLPF is utilized to process VFCI in the frequency domain. GLPF can be described as follows:

$$H(u,v) = e^{-D^{2}(u,v)/2D_0^2} \tag{6}$$

where (u,v) is the row and column of Gaussian low-pass filter, respectively; $D(u,v)$ is the distance between the frequency matrix center and point (u,v); and D_0 is the cut-off frequency.

Applying a GLPF to VFCI enhances the prominence of the vibration data. In order to replicate the curve depicted in the filtered VFCI, it is necessary to implement grading on the remaining data for normalization purposes. The initial step involves summing the three consecutive values within a single column. If the sum of the three values is at its maximum, the three pixel values will be retained while all others are reset to 0. If all values in the column are 0 following GLPF, no action is taken, and the state is maintained. The grading model is outlined as follows:

$$G_v\begin{bmatrix}E_{u+3}\\E_{u+2}\\E_{u+1}\end{bmatrix} = \begin{cases} MAX\left(\sum_{\tau=1}^{3} E_{(\tau+u,v)}\right) & E_{all} \neq 0 \\ NULL & E_{all} = 0 \end{cases} \tag{7}$$

where (u,v) is the row and column of VFCI, respectively, $G_v\begin{bmatrix}E_{u+3}\\E_{u+2}\\E_{u+1}\end{bmatrix}$ are the 3 grading values of VFCI in column v, MAX is the maximum function, and E_{all} is the total value in column v.

$G_v\begin{bmatrix}E_{u+3}\\E_{u+2}\\E_{u+1}\end{bmatrix}$ are the values that remain after the aforementioned processing. 3 values, E_{u+1}, E_{u+2}, and E_{u+3}, can be obtained for each column. These values are the vibration amplitudes, which vary at different times. To mitigate the influence of the different amplitudes, $G_v\begin{bmatrix}E_{u+3}\\E_{u+2}\\E_{u+1}\end{bmatrix}$ is normalized in each column. The maximum value in $G_v\begin{bmatrix}E_{u+3}\\E_{u+2}\\E_{u+1}\end{bmatrix}$ is 2, while the other two values are 1, implying that the grading includes 1 and 2.

4) Gyro frequency information after fitting

The denoised VFCI involves discretizing the image into initial two-dimensional gyroscopic curves for each column, which represent the frequency information of the gyro. Subsequently, multiple frequency curves are individually fitted with segments of parabolas. The equation for the parabolic fitting is presented as follows:

$$f_i(x_i) = b_{i0} + b_{i1}x_i + b_{i2}x_i^2 \tag{8}$$

where $i = 1,2,3,\cdots,M$ is the number of frequency curve segments; $f_i(x_i)$ is the fitting result; x_i is the frequency value; and b_{i0}, b_{i1}, and b_{i2} are the fitting coefficients.

Following the fitting process, the ultimate value for the frequency of each segment is $-\frac{b_{i1}}{2b_{i2}}$, representing the maximum value of the particular segment's frequency curve. This value represents the segment's frequency, with the corresponding amplitude being $b_{i0} - \frac{b_{i1}^2}{4b_{i2}}$.

2.3 Modeling analysis

The vibration of satellite platforms comprises two components: noise and regular signals. Modeling the initial segment is challenging, and at present, predominantly isolation methods are employed to mitigate its effects. The second component is represented by a sine function and can be mathematically expressed using trigonometric functions, as demonstrated in Equation (9):

$$V = asin\left(\frac{2\pi}{f}t + \theta\right) + l \tag{9}$$

where V is the platform vibration result; a is the vibration amplitude; f is the vibration frequency θ is the vibration phase; and l is the vibration constant.

However, platform vibration does not follow a single, simple sine function. Instead, the vibration frequency and amplitude vary, and the platform vibration results from a combination of multiple sine functions. The frequency and amplitude vary according to a sinusoidal function, and can be determined as follows:

$$\begin{cases} f(t) = a_f sin(\omega_f t + \theta_f) + l_f \\ A(t) = a_A sin(\omega_A + \theta_A) + l_A \end{cases} \quad (10)$$

where $f(t)$ and $A(t)$ are the frequency and amplitude results; a_f and a_A are the amplitude of frequency and amplitude changing; ω_f and ω_A are the factors related to frequency of frequency and amplitude changing; θ_f and θ_A are the phase of frequency and amplitude changing; and l_f and l_A are the constants of frequency and amplitude changing.

Subsequently, the satellite platform vibration model can be expressed as follows:

$$V = (a_A sin(\omega_A t + \theta_A) + l_A) sin\left(\frac{2\pi}{a_f sin(\omega_f + \theta_f) + l_f} t + \theta\right) + l \quad (11)$$

This equation represents the long-period satellite vibration model, characterized by its complexity and regularity.

3. Experiment result and discussion

3.1 Gyro raw data

To develop a more intricate and thorough vibration model for the ZY-3 satellite platform, gyro data from the entire cycle of the satellite platform were utilized for vibration analysis and modeling. This study utilizes the raw gyro data collected from February 2012 to February 2021, spanning a decade. The data is obtained from three orthogonally mounted gyros, namely Gyro 1, Gyro 3, and Gyro 5, which are activated in real-time onboard. For each year, 60 tracks were utilized for the satellite platform vibration detection experiment, with 5 tracks being used each month. The experiment was modeled to analyze long-period frequency changes. Taking the gyro data with the identifier (ID) 000489 as an illustrative example (randomly selected), its unprocessed data is depicted in Fig.4. In this figure, the horizontal axis denotes the quantity of gyro data points, while the vertical axis represents the gyro's value, measured in radians per second.

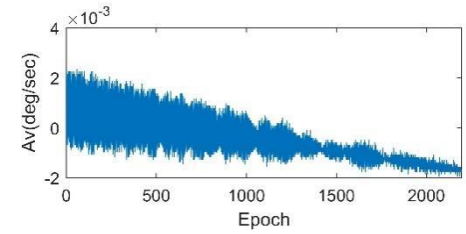

(a) Gyro 1

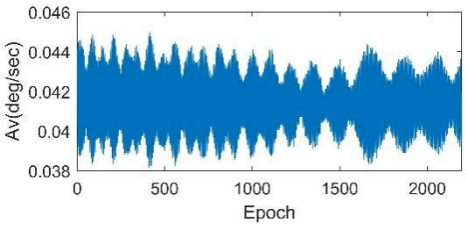

(b) Gyro 3

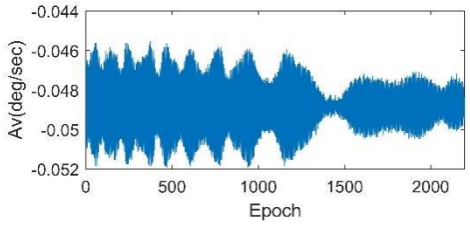

(c) Gyro 5

Figure.4 Gyro raw data analysis from 000489.

3.2 Frequency information in gyro raw data

The gyro data in the satellite body coordinates is considered more appropriate for detecting vibrations. Therefore, all gyro data selected based on time consistency and platform stability is converted into the corresponding satellite body coordinates. Polynomial fitting is utilized to analyze the gyro data from the ZY-3 satellite, as described by Equation (4), in order to mitigate the impact of linear variations. The fitted data is subsequently subjected to FFT analysis to examine the frequency domain data, yielding a two-dimensional spectral graph as depicted in Figure.5. The horizontal axis depicts frequency, and with the ZY-3 satellite's data collection frequency set at 4 Hz, its frequency domain detection range spans from 0 Hz to 2 Hz. The vertical axis depicts amplitude in arcseconds, and the two-dimensional spectral graph can convey the frequency domain information of the original gyro.

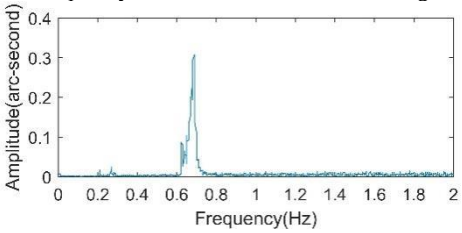

(a) Gyro 1

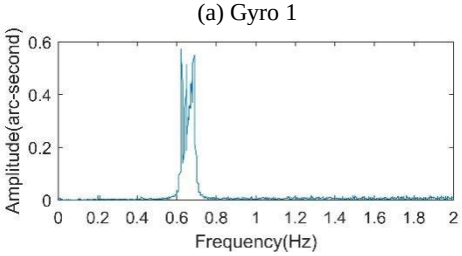

(b) Gyro 3

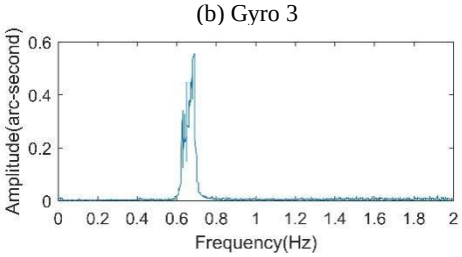

(c) Gyro 5

Figure.5 Frequency curve of gyro raw data from 000489.

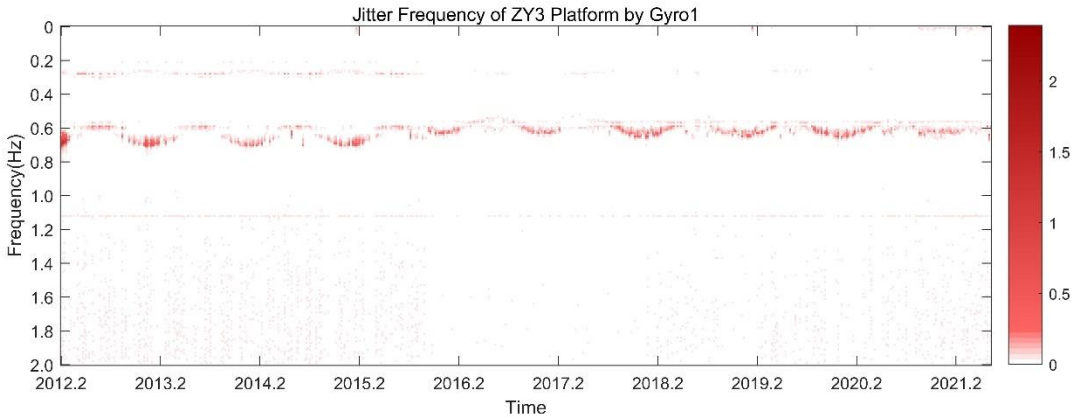

(a) Gyro 1

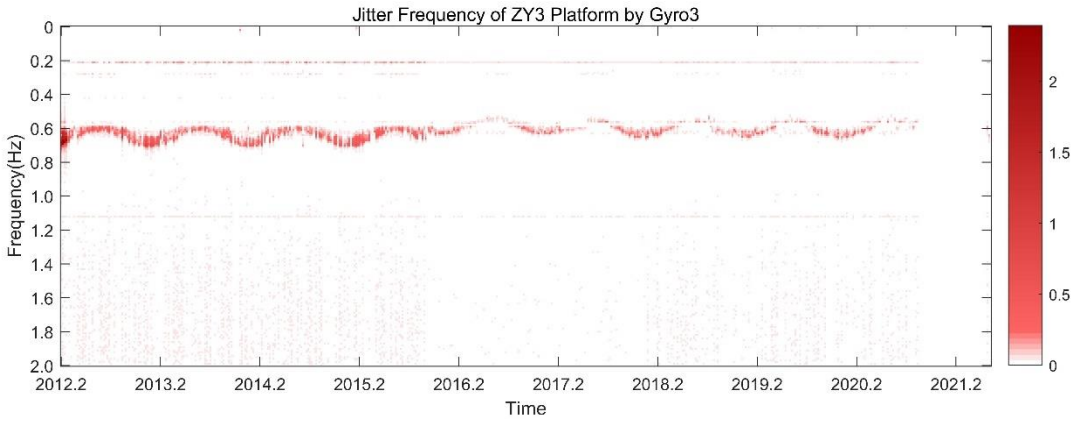

(b) Gyro 3

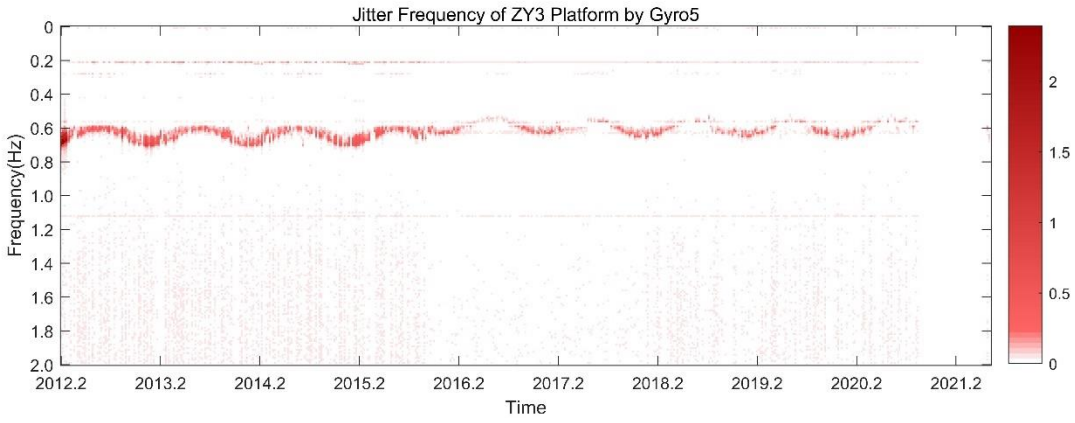

(c) Gyro 5

Figure.6 VFCI analysis of the ZY-3 gyro.

The analysis of Figure.5 reveals that the primary frequency range for the ZY-3 Satellite 01, based on the data of track 000489, is 0.6-0.7 Hz. Due to variations in the installation positions of each gyro and platform, each gyro is capable of measuring angular changes in only one direction. This leads to different gyro spectra with identical frequencies but differing amplitudes.

3.3 VFCI

While a two-dimensional spectral graph is limited to depicting frequency changes over a short period, a technique involving the superimposition of two-dimensional spectra onto a three-dimensional VFCI is employed to represent vibration changes and identify long-term frequency domain changes. This method is designed to capture long-term changes in vibration and frequency. Processing 624 sets of gyro data collected between February 2012 and June 2021, two-dimensional spectral graphs are integrated into a three-dimensional VFCI of the ZY-3 Satellite 01. In this representation, columns depict gyro frequency, while rows correspond to specific time intervals, as illustrated in Figure.6.

As shown in Figure.6, the ZY-3 satellite gyro predominantly operates at frequencies of approximately 0.2 Hz, 0.6 Hz, and 1.1 Hz, with the frequencies around 0.3 Hz and 0.6 Hz displaying sinusoidal variations. A shift in frequency took place on October 15, 2015, as a result of a malfunction in one of the satellite's solar panels, which hindered regular operation and resulted in a discernible alteration in the vibration frequency of the satellite platform. The amplitude of the frequency changes was initially high, primarily due to the activation of various devices on the satellite within the first three months after launch. Additionally, the satellite was in a testing stage, leading to abnormal vibration amplitudes caused

by platform sway. Subsequently, the amplitude began to stabilize. However, there was a decrease in the overall amplitude at the time of the solar panel malfunction.

As the two-dimensional spectrum encompasses both low-frequency vibration data and high-frequency noise, the presence of this noise can impact the development of the frequency domain variation model. Consequently, prior to modeling, it is essential to preprocess VFCI. A GLPF is employed to process VFCI data across a range of treatments. The characteristic of GLPF is that it exhibits maximum value at the center and gradually decreases, thereby enhancing the prominence of the processed VFCI data. To enhance noise reduction in VFCI, a multi-segment parabolic fitting process is applied to each column of VFCI. This process retains the signals within the parabolas (those that are horizontally within) while excluding the external ones.

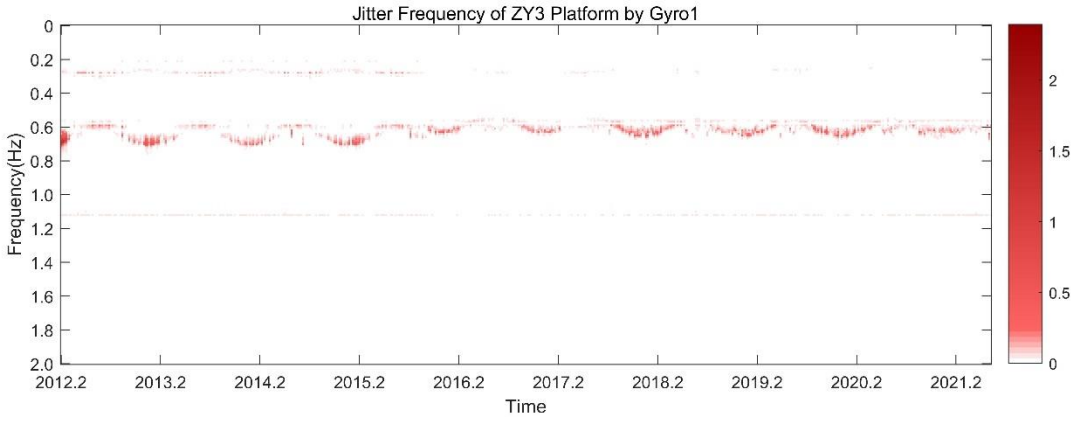

(a) Gyro 1

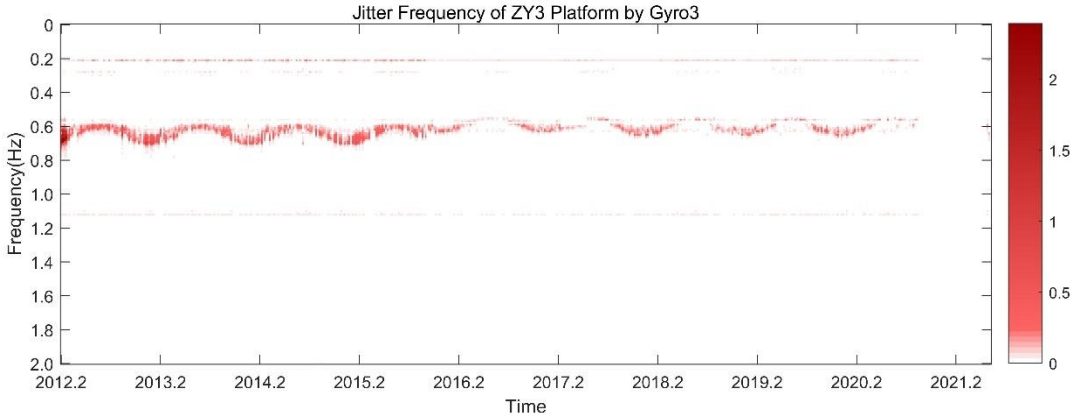

(b) Gyro 3

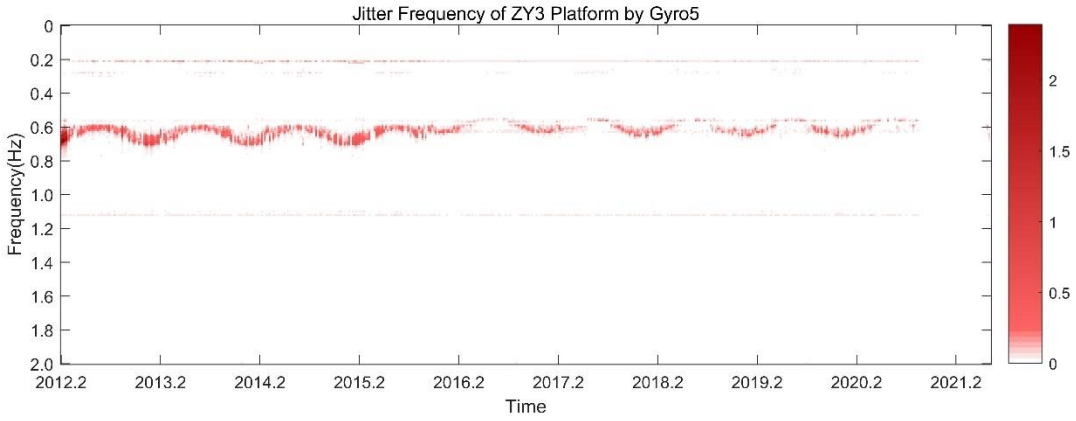

(c) Gyro 5

Figure.7 VFCI for the ZY-3 gyro after denoising process.

After the denoising process, the effective vibration frequencies in VFCI become more discernible, and certain irregular noise is eliminated, thereby enhancing its suitability for fitting with sine functions.

3.4 Frequency and amplitude model building

The denoised VFCI indicates the presence of three stable frequencies at 0.21 Hz, 0.56 Hz, and 1.12 Hz, with corresponding amplitudes of 0.07 ″, 0.04 ″, and 0.04 ″, respectively. The frequencies at approximately 0.3 Hz and 0.6-0.8 Hz exhibit sinusoidal periodic variations. The malfunction of the solar panels resulted in significant changes in frequency segments, requiring the use of two sine curves for fitting. During the latter fitting process, it was observed that achieving high-precision fitting using a single trigonometric function is challenging, particularly when the frequency of the latter segment is gradually changing. In order to more accurately

align with the curve, three functions were employed for fitting in the second segment.

Because Gyro 1, Gyro 3, and Gyro 5 are all securely attached to the same satellite platform, the readings from the three gyros demonstrate uniformity. Consequently, in the process of fitting, the three sets of data from the same time period are consistently fitted using a single set of parameters for all three data sets, as illustrated in Figure.8.

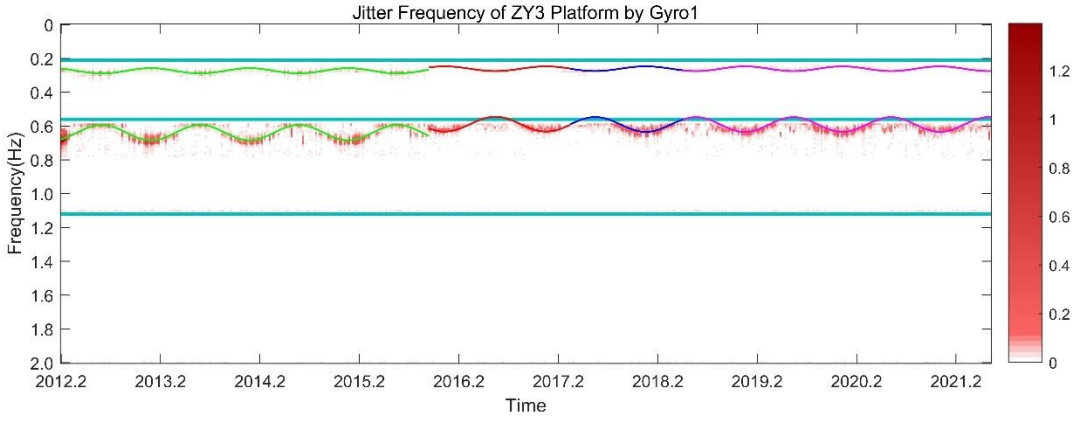

(a) Gyro 1

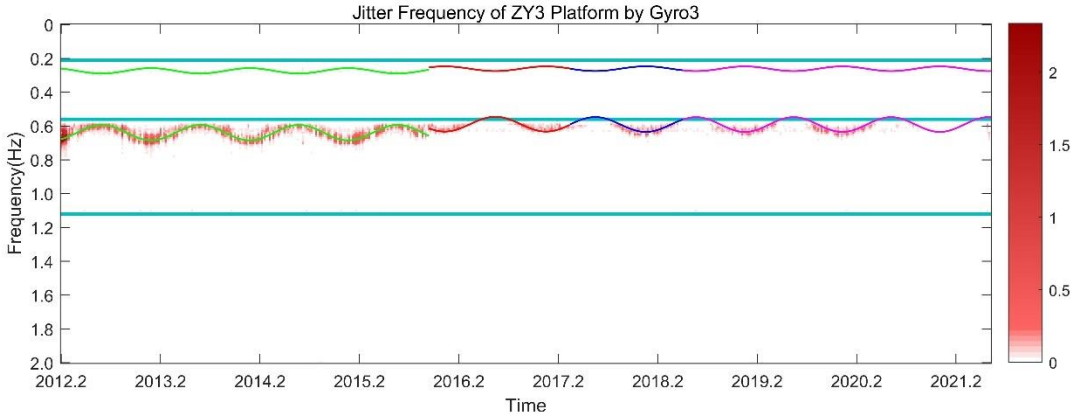

(b) Gyro 3

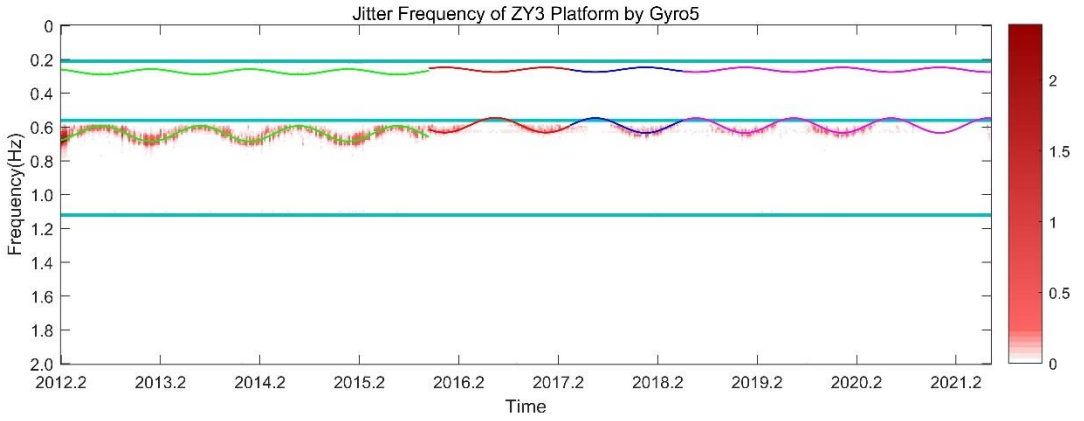

(c) Gyro 5

Figure.8 Curve fitting analysis of the ZY-3 gyro's VFCI.

As depicted in Figure.8, three green straight lines respectively fit the three fixed frequencies of 0.21 Hz, 0.56 Hz, and 1.12 Hz. The cyan curve fits the first segment (February 2012 to October 2015) frequency, the red curve fits the second segment (October 2015 to April 2017), the blue curve fits the third segment (May 2017 to May 2017), and the burgundy curve fits the fourth segment (June 2017 to May 2021). The fitting information is shown in Table 1.

The further examination of the amplitude at a frequency of 0.3 Hz entails aggregating the amplitudes between 0.23 Hz and 0.4 Hz by column and presenting them in chronological sequence. The amplitude derived from the three sets of gyro data is modeled using a trigonometric function, leading to the representation of the vibration amplitude change curve depicted in Figure.9. The amplitude of frequency for the three sets of gyro remains consistent, exhibiting an increase during the initial stages of orbit and a significant reduction following the malfunction of the solar panel. The amplitudes and periods of the three gyros before and after are 361 days. The first segment's amplitude averages 0.03″ and remains constant at 0.06″, while the second segment's amplitude averages 0.01″ and remains constant at 0.05″.

The additional analysis of the amplitude at a frequency of 0.6 Hz entails aggregating the amplitudes between 0.57 Hz and 0.8 Hz by column and presenting them in chronological sequence. The amplitude derived from the three sets of gyro data is

modeled using a trigonometric function, leading to the vibration amplitude change curve depicted in Figure.10. The amplitude periods of the three gyros before and after are 361 days. The amplitude of the first segment is 0.28″ and remains constant at 0.34″, while the second segment's initial amplitude is 0.15″ and remains constant at 0.33″.

Table 1. Frequency change model parameters for the ZY-3 satellite

Period/day		First Segment	Second one	Third one	Fourth one
		361	371	369	357
Amplitude/Hz	0.3Hz	0.016	0.014	0.014	0.014
	0.6Hz	0.046	0.044	0.044	0.044
Constant/Hz	0.3Hz	0.283	0.271	0.271	0.271
	0.6Hz	0.649	0.599	0.601	0.601

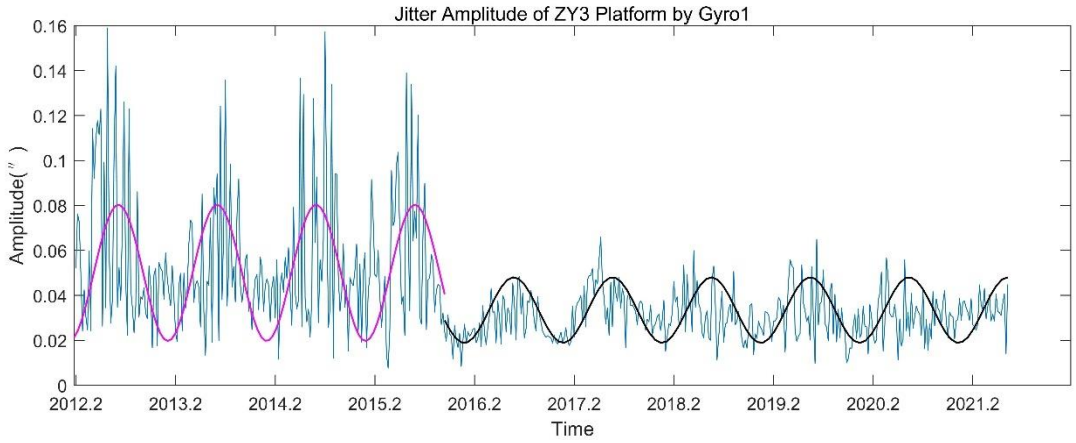

(a) Gyro 1

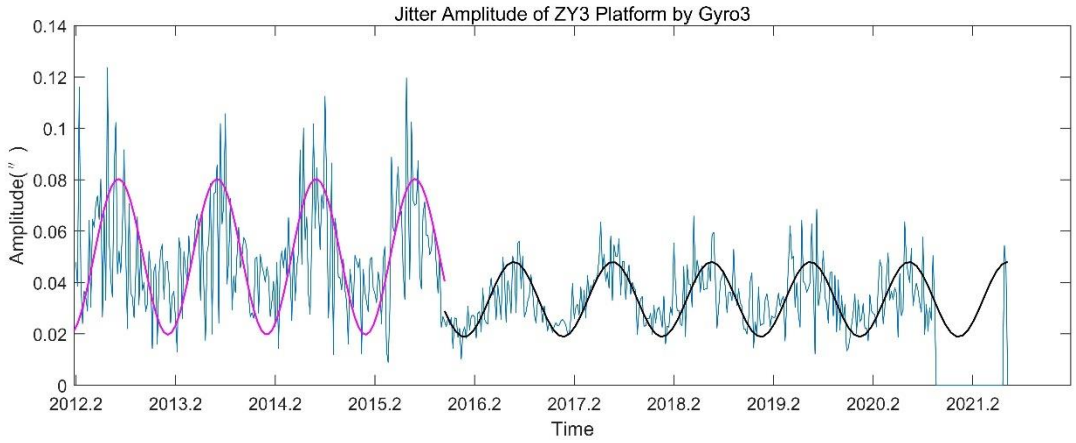

(b) Gyro 3

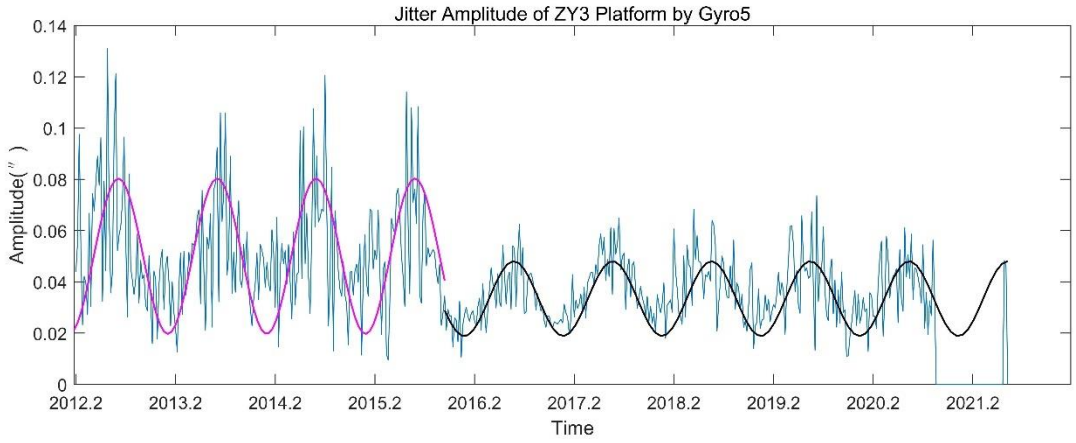

(c) Gyro 5

Figure.9 Amplitude variations at 0.3 Hz frequency range.

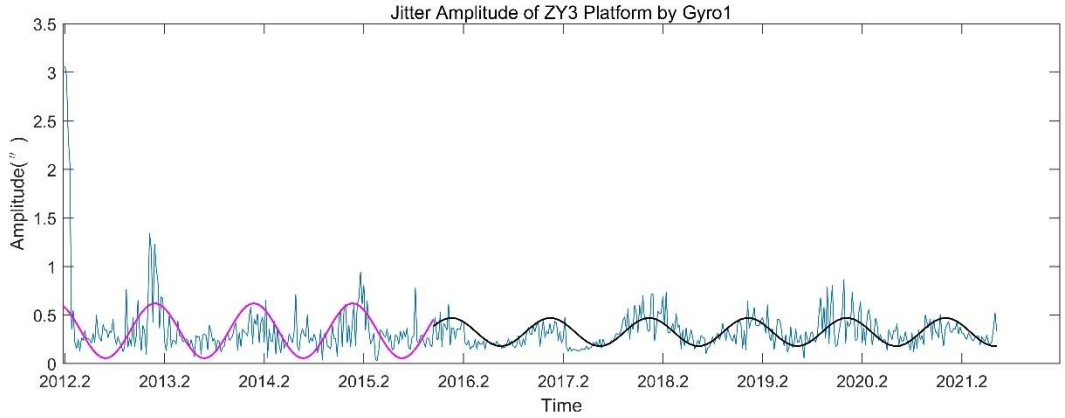

(a) Gyro 1

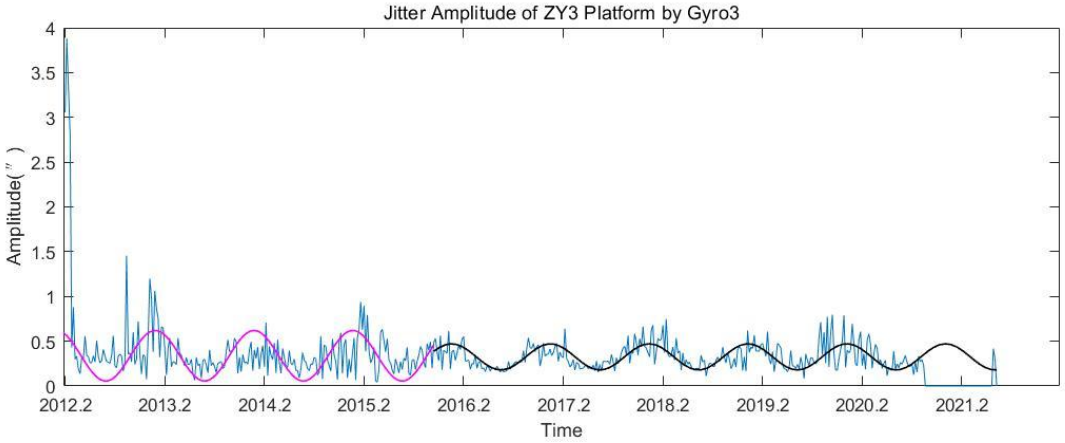

(b) Gyro 3

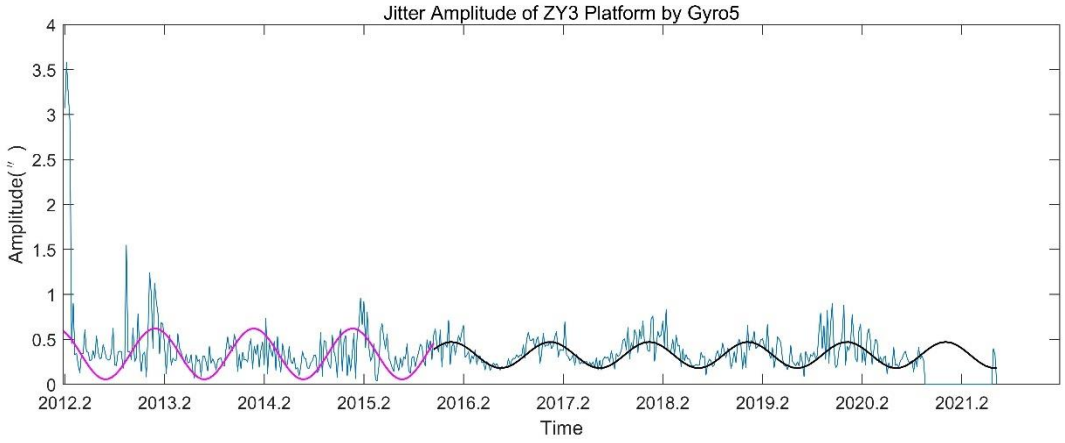

(c) Gyro 5

Figure.10 Amplitude variations at 0.6 Hz frequency range

The results presented above facilitate the derivation of the amplitude model's various parameters, as outlined in Table 2. Upon inputting the frequency change parameters and amplitude parameters into Equation (11), the comprehensive vibration model for the ZY-3 satellite platform's entire lifecycle can be established.

Table 2. Amplitude model parameters for frequency change

Period/day		First Segment	Second one
		361	
Amplitude/″	0.3Hz	0.03	0.06
	0.6Hz	0.28	0.15
Constant/″	0.3Hz	0.01	0.05
	0.6Hz	0.34	0.33

3.5 Discussion

The analysis of the gyro data from the ZY-3 satellite indicates that the platform vibration demonstrates consistent regularity over the satellite's entire lifecycle, with its frequency gradually changing over time. As depicted in Figure.8, following a malfunction in the solar panels on one side of the satellite, discernible alterations in the vibration frequency around 0.3 Hz and 0.6 Hz were observed, predominantly marked by a decrease in vibration amplitude. This illustrates the substantial influence of the operational condition of the solar panels on the satellite platform. The solar panels must be able to adjust their orientation in real time to track the sun, and the resulting torque causes vibrations in the platform. This indicates that

solar panels make a substantial contribution to the vibration of satellite platforms. This aspect warrants attention in the development of satellites. Following the malfunction of the solar panel, the frequency was not rectified but instead divided into three segments, which gradually increased. This may be linked to the performance of the satellite's payload. The vibration of the satellite platform is characterized by three fixed frequency regions: 0.21 Hz, 0.56 Hz, and 1.12 Hz, each with corresponding amplitudes of 0.07″, 0.04″, and 0.04″, respectively. This phenomenon could be attributed to the continuous operation of specific payloads within the satellite, such as star sensors and gyros. As indicated in Tables 1 and 2, the periods of frequency and amplitude exhibit a strong correlation with the annual cycle, which is likely associated with the influence of solar radiation pressure. During the winter season, the satellite is situated at a greater distance from the sun, resulting in a decrease in force and more significant alterations in frequency and amplitude. Conversely, in the summer months, the satellite is closer to the sun, leading to an increase in force and subsequently smaller changes in frequency and amplitude.

The amplitude of the vibration frequency near 0.3 Hz on the satellite platform exhibited significant changes before and after the solar panel malfunction, as depicted in Figure.9. However, in Fig.10, the change around the time of the solar panel fault is less pronounced. This indicates that the solar panels have a primary impact on the magnitude of the vibration frequency around 0.3 Hz. When combined with Figure.8, it becomes apparent that there is also an influence at 0.6 Hz, primarily in the steady-state component. Following the malfunction, the amplitude of the vibration frequency did not demonstrate a change in frequency as depicted in Figure.8. This suggests that a single curve may adequately fit the data, indicating that the amplitude may not be influenced by the decrease in payload performance towards the end of the satellite's operational life. Table 2 indicates that the amplitude and constant of the initial segment at approximately 0.3 Hz are double those of the subsequent segment. This suggests that following the malfunction of the solar panel, the alteration in this frequency was reduced by half, providing additional evidence that the solar panels predominantly impact this frequency range. The amplitude at approximately 0.6 Hz decreased by half, while the constant remained relatively unchanged. This suggests that the malfunction impacted the variability of this frequency but not its baseline. In Figure.9 and 10, during the initial and final stages of the satellite's orbit, the influence on the frequency around 0.3 Hz is negligible, whereas a variation is observed at 0.6 Hz. The different payload function tests conducted during the initial stages of orbit resulted in an increased frequency at this juncture. Upon achieving orbit stabilization, the satellite entered a relatively stable stage, suggesting that maneuvers such as orbit adjustment, focusing, and yawing primarily impact the frequency at this stage.

4. Conclusion and future work

The vibration of satellite platforms is a critical concern that impacts the imaging quality of stereo cameras and the precise measurement of satellite attitude. This study employed a decade of original gyro data from the ZY-3 satellite to identify vibrations and developed a model for long-period frequency changes in satellite platform vibration. The analysis identified three fixed frequencies of vibrations at 0.21 Hz, 0.56 Hz, and 1.12 Hz, each with corresponding amplitudes of 0.07″, 0.04″, and 0.04″. Additionally, two fluctuating frequencies were observed in close proximity to 0.3 Hz and 0.6 Hz. The paper conducted experiments to detect vibrations and identified the long-term patterns of vibration variation in the ZY-3 satellite. It also analyzed the relationship between different frequencies and the payloads on the platform. A comprehensive vibration model for the ZY-3 satellite platform was developed using frequency and amplitude functions obtained from experimental analysis. This model serves as a mathematical framework for guiding future satellite platform development, optimizing attitude determination accuracy, and enhancing image quality.

The future research directions of this paper include investigating the to mitigate their influence on the platform. Furthermore, this study made use of a substantial volume of gyro data. As a result of the limited gyro data transmitted by the ZY-3 satellite, which is only available during camera operation periods, the scope of vibration analysis is constrained to these specific time frames. This limitation hinders comprehensive orbit analysis and, although it permits analysis of annual cycle frequencies, it overlooks the influence of the orbital period on the vibration model. Subsequently, the authors intend to utilize gyro data from other satellites transmitted throughout the entire orbit to perform vibration analysis experiments for orbital periods and enhance the vibration model.

Declaration of Competing Interest

The authors declare that they have no known competing financial interests or personal relationships that could have appeared to influence the work reported in this paper.

Acknowledgments

This work was supported by the National Natural Science Foundation of China (No. 42001416). Technology Innovation Center for Spatio-temporal Information and Equipment of Intelligent City, MNR (No. STIEIC-KF202308). Independent research program of key Laboratory of Land Satellite Remote Sensing Application, MNR (No.BN2302-6).

References

Ayoub F, Leprince S, Binet R, et al. Influence of camera distortions on satellite image registration and change detection applications[C]//IGARSS 2008-2008 IEEE International Geoscience and Remote Sensing Symposium.IEEE,2008:II-1072-II-1075.

Cao H, Liu X, Li S, et al. 2012. ZY-3 Satellite Remote Sensing Technology. SPACECRAFT RECOVERY & REMOTE SENSING [J], 33: 7-16.

Chen J, Yang J-G, An W, et al. 2017. An Attitude Jitter Correction Method for Multispectral Parallax Imagery Based on Compressive Sensing. IEEE Geoscience and Remote Sensing Letters [J], 14: 1903-1907.

Chen J, ZHOU Y-q, LI C-s, et al. 2001. Relationship between satellite attitude jitter and SAR imaging quality. Journal of Beijing University of Aeronautics and Astronautics [J], 27: 518-521.

Gao h, Luo W, Shi H, et al. 2016. Structural Stability Design and Implementation of ZY-3 Satellite. SPACECR AFT ENGINEERING [J], 25: 18-24.

Guo C, Tong X, Liu S, et al. 2017. High-precision attitude estimation method of star sensors and gyro based on

complementary filter and unscented Kalman filter. The International Archives of the Photogrammetry Remote Sensing Spatial Information Sciences [J], 42: 49-53.

Kirk R L, Howington-Kraus E, Rosiek M R, et al. 2008. Ultrahigh resolution topographic mapping of Mars with MRO HiRISE stereo images: Meter-scale slopes of candidate Phoenix landing sites. Journal of Geophysical Research: Planets [J], 113.

Liu S, Tong X, Wang F, et al. 2016. Attitude Jitter Detection Based on Remotely Sensed Images and Dense Ground Controls: A Case Study for Chinese ZY-3 Satellite. Ieee Journal of Selected Topics in Applied Earth Observations and Remote Sensing [J], 9: 5760-5766.

Mattson S, Bartels A, Boyd A, et al. Continuing analysis of spacecraft jitter in LROC-NAC[C]//42nd Annual Lunar and Planetary Science Conference.2011:2756.

Mo F, Xie J, Liu Y 2020. Vibration model of Ziyuan3 satellites considering frequency changing. Journal of Vibration and Control [J], 26: 1484-1502.

Pan J, Che C, Zhu Y, et al. 2017. Satellite Jitter Estimation and Validation Using Parallax Images. Sensors [J], 17.

Sun T, Long H, Liu B-C, et al. 2015. Application of at titude jitter detection based on short-time asynchronous i mages and compensation methods for Chinese mapping s atellite-1. Optics Express [J], 23: 1395-1410.

Tang X, Zhang G, Zhu X, et al. 2013. Triple linear-arra y image geometry model of ZiYuan-3 surveying satellite and its validation. International Journal of Image Data F usion [J], 4: 33-51.

Teshima Y, Iwasaki A 2007. Correction of attitude fluctuation of Terra spacecraft using ASTER/SWIR imagery with parallax observation. IEEE Transactions on Geoscience Remote Sensing [J], 46: 222-227.

Tong X, Li L, Liu S, et al. 2015a. Detection and estimation of ZY-3 three-line array caused by attitude oscillation. Isprs Journal of Photogrammetry and Remote Sensing [J], 101: 291-309.

Tong X, Xu Y, Ye Z, et al. 2015b. Attitude Oscillation Detection of the ZY-3 Satellite by Using Multispectral Parallax Images. IEEE Transactions on Geoscience and Remote Sensing [J], 53: 3522-3534.

Tong X, Ye Z, Liu S 2017. Essential Technology and Application of Jitter Detection and Compensation for High Resolution Satellite. Acta Geodaetica et Cartographica Sinica [J], 46: 1500-1508.

Tong X, Ye Z, Liu S, et al. 2018. Jitter Detection for High Resolution Satellite Based on Phase Correlation with Local Frequency Analysis. Acta Geodaetica et Cartographica Sinica [J], 47: 1346-1352.

Tong X, Ye Z, Xu Y, et al. 2014. Framework of Jitter Detection and Compensation for High Resolution Satellites. Remote Sensing [J], 6: 3944-3964.

Toyoshima M, Takayama Y, Kunimori H, et al. 2010. In-orbit measurements of spacecraft microvibrations for satellite laser communication links. Optical Engineering [J], 49: 083604-083604-083610.

Wang M, Fan C, Pan J, et al. 2017. Image jitter detection and compensation using a high-frequency angular displacement method for Yaogan-26 remote sensing satellite. Isprs Journal of Photogrammetry and Remote Sensing [J], 130: 32-43.

Wang M, Zhu Y, Jin S, et al. 2016. Correction of ZY-3 image distortion caused by satellite jitter via virtual steady reimaging using attitude data. Isprs Journal of Photogrammetry and Remote Sensing [J], 119: 108-123.

Xiong K, Liang T, Yongjun L 2011. Multiple model Kalman filter for attitude determination of precision pointing spacecraft. Acta Astronautica [J], 68: 843-852.

Ye Z, Xu Y, Tong X, et al. 2019. Estimation and analysis of along-track attitude jitter of ZiYuan-3 satellite based on relative residuals of tri-band multispectral imagery. Isprs Journal of Photogrammetry and Remote Sensing [J], 158: 188-200.

Ye Z, Xu Y, Zheng S, et al. 2020. Resolving time-varying attitude jitter of an optical remote sensing satellite based on a time-frequency analysis. Optics Express [J], 28.

Yuan R, Song N, Jin J 2012. Autonomous estimation of angle random walk of fiber optic gyro in attitude determination system of satellite. Measurement [J], 45: 1362-1366.

Zhang H, Ye Z, Liu S, et al. 2018. Detection and Compensation of Attitude Jitter for ZY-3 Satellite Based on Virtual Control Point. Journal of Lanzhou Jiaotong University [J], 37: 143-148.

Zhu Y, Wang M, Pan J, et al. 2015. Deteciton of ZY-3 Satellite Platform Jitter Using Multi-spectral Imagery. Acta Geodaetica et Cartographica Sinica [J], 44: 399-406+413.